Journal of
Synchrotron Radiation

ISSN 1600-5775

Received 8 August 2014
Accepted 18 November 2014

A new extra-focus monochromator designed for high-performance VUV beamlines

Chaofan Xue, Yanqing Wu,* Ying Zou, Lian Xue, Yong Wang,* Zijian Xu and Renzhong Tai*

Shanghai Institute of Applied Physics, Chinese Academy of Sciences, Shanghai Synchrotron Radiation Facility, Shanghai 201800, People's Republic of China.
*E-mail: wuyanqing@sinap.ac.cn, wangyong@sinap.ac.cn, tairenzhong@sinap.ac.cn

A new monochromator called an extra-focus constant-included-angle varied-line-spacing (VLS) cylindrical-grating monochromator (extra-focus CIA-VCGM) is described. This monochromator is based on the Hettrick–Underwood scheme where the plane VLS grating is replaced by a cylindrical one in order to zero the defocus at three reference photon energies in the vacuum-ultraviolet range. It has a simple mechanical structure and a fixed focus spot with high performance over a wide energy range. Furthermore, its mechanical compatibility with a standard VLS plane-grating monochromator allows convenient extension into the soft-X-ray range.

Keywords: VUV beamline; monochromator.

1. Introduction

The design of synchrotron optics depends on many factors. Soft X-ray and vacuum-ultraviolet (VUV) monochromators are particularly challenging as they rely on two-dimensional man-made gratings as opposed to self-organized three-dimensional crystal structures that can be used for hard X-rays. As a result, VUV beamlines around the world that employ these monochromators are forced to make compromises that limit their performance and/or flexibility. Special techniques, such as using a varied-included-angle plane-grating monochromator (VIA-PGM) (Petersen, 1982; Riemer & Torge, 1983; Pimpale *et al.*, 1991) and extra-focus constant-included-angle varied-line-spacing plane-grating monochromator (extra-focus CIA-VPGM) (Hettrick & Bowyer, 1983; Hettrick & Underwood, 1986; Hettrick *et al.*, 1988) have been developed for soft X-rays to achieve high performance in terms of energy resolution, flux and flexibility. Nevertheless, these techniques are challenged in the VUV range.

Here we describe a new VUV monochromator approach well suited for experiments demanding high performance, such as angle-resolved photoemission spectroscopy (ARPES), photoelectron emission microscopy (PEEM) *etc.* The ARPES method is a powerful technique that characterizes electrons' properties close to the Fermi surface in materials (Tanaka *et al.*, 2006; Terashima *et al.*, 2006; Damascelli & Shen, 2003). The escape length of photoelectrons emitted in solid materials exhibits the famous 'V-curve' relation with their kinetic energy (Somorjai, 1981). It reaches the minimum of approximately 1 nm at photon energies from 10 eV to 200 eV, which limits the ability to obtain interior information from a sample. Such surface sensitivity can be circumvented by tuning the photon energy higher (soft X-ray > 1000 eV) or lower (VUV < 10 eV). Owing to its higher energy resolving power, the VUV route is favoured for ARPES beamlines.

At present, many types of monochromators are utilized for ARPES beamlines. The VIA-PGM type (Strocov *et al.*, 2010; Songsiriritthigul *et al.*, 2003; Xue *et al.*, 2014) which can cover a wide energy range can be operated in different modes according to the experimental requirements. A normal-incidence monochromator (NIM) type that can operate in the VUV range has been adopted by many beamlines (Rah *et al.*, 1995; Janowitz *et al.*, 2012; Petaccia *et al.*, 2009). The fixed exit slit of the NIM can always maintain a small spot size on samples, which is required for new nano-ARPES technology (Bostwick *et al.*, 2012). Moreover, a small spot size is necessary to handle some novel samples, which are usually tiny in size. A combination of the VIA-PGM type and the NIM type can cover a wider photon energy range from VUV to soft X-ray (Borisenko, 2012). The dragon type is another typical choice for the VUV range and has been mounted in many beamlines (van Elp, 1997; Yu *et al.*, 2001; Lai *et al.*, 2001) since it is a high-performance (high energy resolution and high photon flux) monochromator. A constant-length Rowland monochromator (Reininger *et al.*, 2007), with a moving range of 1.1 m of the pre-mirror, was designed to obtain a fixed exit slit by setting a plane mirror before the spherical grating and varying the incidence angle on the plane mirror to fulfil the Rowland condition.

An extra-focus CIA-VPGM monochromator type (Hettrick–Underwood scheme) has already been employed by many beamlines (Kiyokura *et al.*, 1998; Ono *et al.*, 2001; Yan *et al.*, 1998; Underwood & Gullikson, 1998). It is a high-performance monochromator with a variety of advantages, such as

high energy resolving power, high throughput, a simple scanning mechanism and a fixed exit slit. However, in the VUV range the focus drifts more dramatically because of larger defocus aberration (which will be discussed below). In this study, a modified Hettrick–Underwood scheme based monochromator with a simple mechanical structure is designed. The plane varied-line-spacing (VLS) grating in an extra-focus CIA-VPGM type is suggested to be replaced by a cylindrical one. With this change, the advantages of the extra-focus CIA-VPGM can be retained in the VUV range. The new-type monochromator (extra-focus CIA-VCGM) will have a fixed focus by suppressing the defocus aberration by an order of magnitude while retaining high energy resolving power and high photon flux. It has the potential to meet the harsh requirements of a high-performance VUV beamline.

2. CIA-VCGM monochromator

For a VLS grating, the line spacing d is a function of the position w in the dispersive direction. The function can be expanded as a power series of w, namely

$$d(w) = d_0\left(1 + b_2 w + b_3 w^2 + b_4 w^3 + \cdots\right), \qquad (1)$$

where d_0 is the line spacing at the centre of the grating, and b_2, b_3 and b_4 are the space-variation parameters. The defocus term (F_{20}) and the coma term (F_{30}) in an optical path function can be eliminated by choosing an appropriate linear coefficient term b_2 and quadratic term b_3, respectively, according to

$$F_{20} = \left(\frac{\cos^2\alpha}{r_1} + \frac{\cos^2\beta}{r_2}\right) - \frac{\cos\alpha + \cos\beta}{R} - b_2\frac{m\lambda}{d_0}, \qquad (2)$$

$$F_{30} = \left(\frac{\sin\alpha\cos^2\alpha}{r_1^2} + \frac{\sin\beta\cos^2\beta}{r_2^2}\right) - \frac{1}{R}\left(\frac{\sin\alpha\cos\alpha}{r_1} + \frac{\sin\beta\cos\beta}{r_2}\right) + \frac{2}{3}\left(b_2^2 - b_3\right)\frac{m\lambda}{d_0}, \qquad (3)$$

where m is the diffraction order, α is the incidence angle, β is the diffraction angle, r_1 is the objective distance, r_2 is the imaging distance and R is the grating radius (for a plane grating, $R \rightarrow \infty$).

In an extra-focus CIA-VPGM type monochromator [$R \rightarrow \infty$ in equation (2)] the focusing mirror produces a converging beam and a virtual source to the grating, and the grating produces a real image on the exit slit with an imaging distance that is almost identical to the virtual source distance. To correct the defocus aberration, certain optimization methods can be applied. The defocus term can be eliminated directly ($F_{20} = 0$) at one reference energy or be approximated equal to zero using $b_2 \simeq 2/r$ (Sinn *et al.*, 2012). Better focusing performance over a wide spectral range (Yan & Yagishita, 1995*a*; Hettrick & Underwood, 1988) eliminates defocus aberration at two specific photon energies. Nevertheless, owing to drastic changes in the focus condition over the VUV energy range it is difficult to effectively suppress the defocus term and this type of monochromator is generally favoured for the soft X-ray or extreme ultraviolet range (Kiyokura *et al.*, 1998; Ono *et al.*, 2001; Yan *et al.*, 1998; Underwood & Gullikson, 1998) but not the VUV range. To extend the photon energy into this range, we replace the plane grating in an extra-focus CIA-VPGM type monochromator with a cylindrical grating (Fig. 1). With this change, a new optimized method can be used to eliminate defocus aberration at three reference energies. The defocus curve of the cylindrical surface can compensate for the defocus behaviour of the VLS grating in the VUV range. In this way the focusing performance can be improved. In the following we will refer to this new type of monochromator as an extra-focus constant-included-angle varied-line-spacing cylindrical-grating monochromator (extra-focus CIA-VCGM).

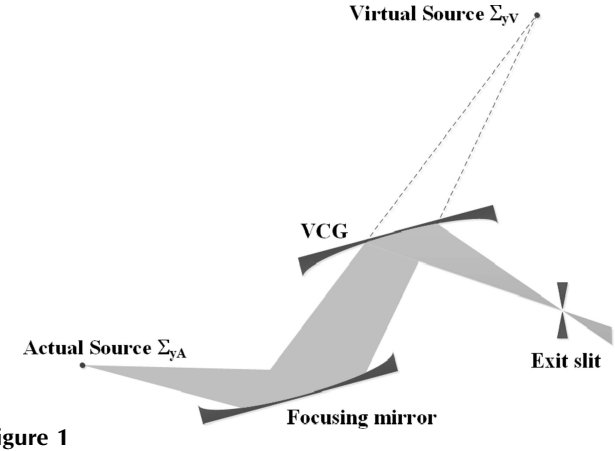

Figure 1
Optical schematic of an extra-focus CIA-VCGM.

The optical schematic of an extra-focus CIA-VCGM is shown Fig. 1. As in an extra-focus CIA-VPGM, the focusing mirror produces a converging beam and a virtual source behind the grating and the grating produces a real image on the exit slit. Yet a major difference is prominent: the imaging distance is not equal to the virtual source distance. In order to illustrate the improved performance of an extra-focus CIA-VCGM, we take a 4 m-long undulator as a realistic optical source and typical distance values between optical elements for a model CIA-VPGM and a model CIA-VCGM as an example comparison. The beam sizes and divergences are calculated from the vector sum of the electron beam RMS values (σ_x, σ_x', σ_y, σ_y') on the orbit and the single electron radiation values (σ_r, σ_r'). The single electron radiation values are calculated using the approximations $\sigma_r = (2\lambda L)^{1/2}/2\pi$ and $\sigma_r' = (\lambda/2L)^{1/2}$, where λ is the wavelength of the radiation and L is the length of the insertion device. For both models, the object distance of the focusing mirror is 20 m and the imaging distance of the grating is 29 m. Two optical elements are separated by 0.5 m. The calculated RMS values of the total photon beam size (Σ_{yA}) and total photon divergence (Σ_{yA}') are shown in Figs. 2(*a*) and 2(*b*). The corresponding full width at half-maximum (FWHM) of the beam spot in the dispersion direction at the exit slit for the model CIA-VCGM is also shown in Fig. 2(*c*). Detailed parameters for the models are listed in Table 1.

The second term at the right-hand side of equation (2) vanishes with an infinite radius R (a plane grating). However,

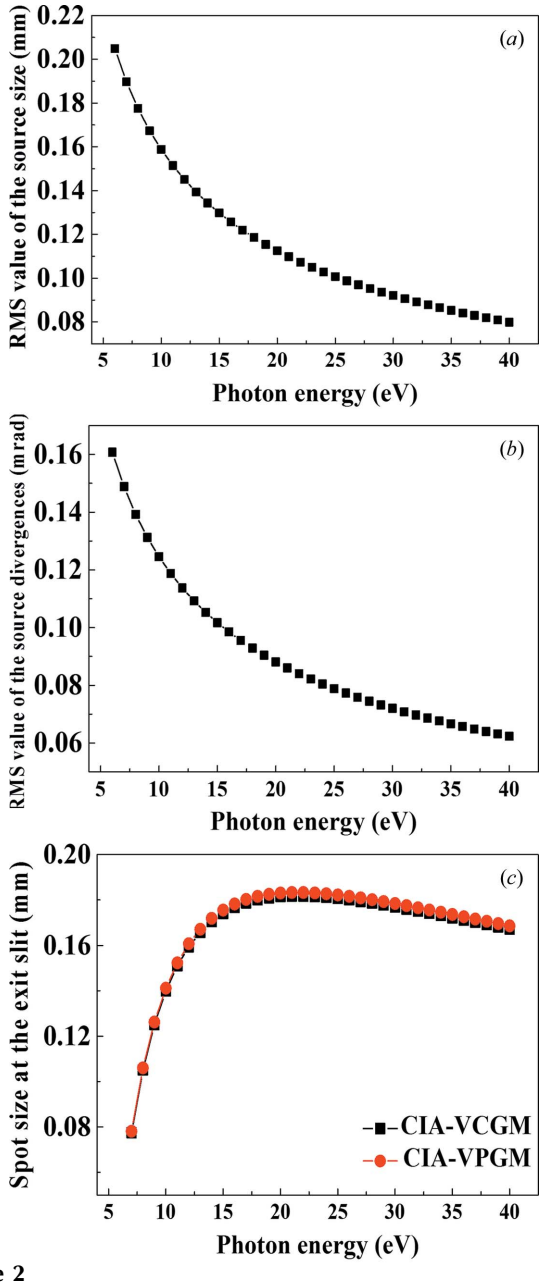

Figure 2
(*a*) RMS values of the total photon beam size (Σ_{yA}). (*b*) RMS values of the total photon beam divergence (Σ'_{yA}) and (*c*) the spot size in the dispersion direction at the exit slit of the model CIA-VCGM.

this term comes into play in the cylindrical grating case because R is no longer infinite. Thus, r_2 (or r_1, one of them should be fixed), b_2 and R can be determined by imposing the condition that F_{20} vanishes at three reference energies, *i.e.* the defocus aberration is simultaneously suppressed at these three reference energies. The criterion for optimizing the model CIA-VCGM is to ensure that the defocus term of the cylindrical surface can effectively compensate that of the varied-line-spacing plane grating (VLS-PG) (Fig. 3) in the VUV range by testing various sets of reference energies. The defocus term of a concave VLS grating in the model CIA-VCGM contains two parts: the defocus of a VLS-PG (Fig. 3, squares), $(\cos^2\alpha/r_1 + \cos^2\beta/r_2) - b_2 m\lambda/d_0$, and the contribution

Table 1
Detailed parameters for the models.

Electron beam RMS size	
Horizontal σ_x (mm)	0.15855
Vertical σ_y (mm)	0.00987
Electron beam RMS divergence	
Horizontal σ'_x (rad)	3.2914×10^{-5}
Vertical σ'_y (rad)	3.9497×10^{-6}
Undulator length (mm)	4000
Focusing mirror slope error (rad)	5×10^{-7}
Object distance of the focusing mirror (mm)	20000
Incident angle of the focusing mirror (°)	20
Distance from the source to the grating (mm)	23500
Grating slope error (rad)	3×10^{-7}
Imaging distance of the grating (mm)	29000
Included angle (°)	140

Table 2
Calculated parameters for the models.

Items	CIA-VCGM	CIA-VPGM†
Virtual source of the grating (mm)	45290	26666
Curvature radius of the focusing mirror (mm)	81399	67360
Curvature radius of grating (mm)	497663	–
b_2 (mm^{-1})	5.56311×10^{-5}	6.24671×10^{-5}
b_3 (mm^{-2})	7.19823×10^{-10}	1.27756×10^{-9}

† The reference energy set here is chosen to be 7 eV and 15 eV.

of the cylindrical surface (Fig. 3, circles), $(\cos\alpha + \cos\beta)/R$. Both parts counteract each other in the VUV range. Therefore, the contribution of the cylindrical surface can effectively compensate for that of the VLS-PG to keep F_{20} very low over the entire VUV range.

The reference energies for the two model monochromators are chosen to make the defocus as small as possible. After optimizing, the defocus vanishes at 7 eV, 8.5 eV and 25 eV and the coma vanishes at 7 eV for the model CIA-VCGM. For the model CIA-VPGM, the defocus aberration is optimized under several different energy sets and the coma vanishes at 7 eV too. The grating line density is assumed to be the same (1000 lines mm^{-1}) in the model. A few parameters can be derived under these conditions and are listed in Table 2.

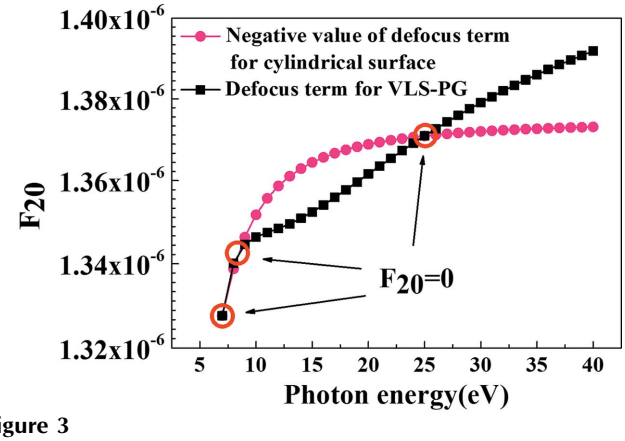

Figure 3
Contributions of the defocus from an extra-focus CIA-VPGM and a cylindrical surface. The defocus vanishes at 7 eV, 8.5 eV and 25 eV.

The energy resolving power (RP) calculated in this study is mainly determined by seven factors: source size, exit slit size, meridian slope error of the grating and focusing mirror, the aberrations from the defocus and coma, and the grating diffraction limit. High-order aberrations (smaller than F_{30}) are small and negligible. Figs. 4(*a*) and 4(*b*) show the calculated RP with various grating line densities of the model monochromator, with the RP defined as the inverse of the relative spectrum width (RSW). Their contributions to the RSW, $\Delta\lambda/\lambda_{\rm total}$, are as follows:

Virtual source size:

$$\Delta\lambda/\lambda_{\rm so} = \frac{2.35d\Sigma_{y\rm V}\cos\alpha}{m\lambda r_1}.$$

Exit slit size:

$$\lambda/\lambda_{\rm ex} = \frac{sd\cos\beta}{m\lambda r_2}.$$

Meridian slopes errors of grating:

$$\lambda/\lambda_{\rm gr} = \frac{2.35d\sigma_{\rm gr}}{m\lambda}(\cos\alpha + \cos\beta).$$

Meridian slopes errors of mirror:

$$\lambda/\lambda_{\rm fo} = \frac{4.7d\sigma_{\rm fo}\cos\alpha}{m\lambda}. \quad (4)$$

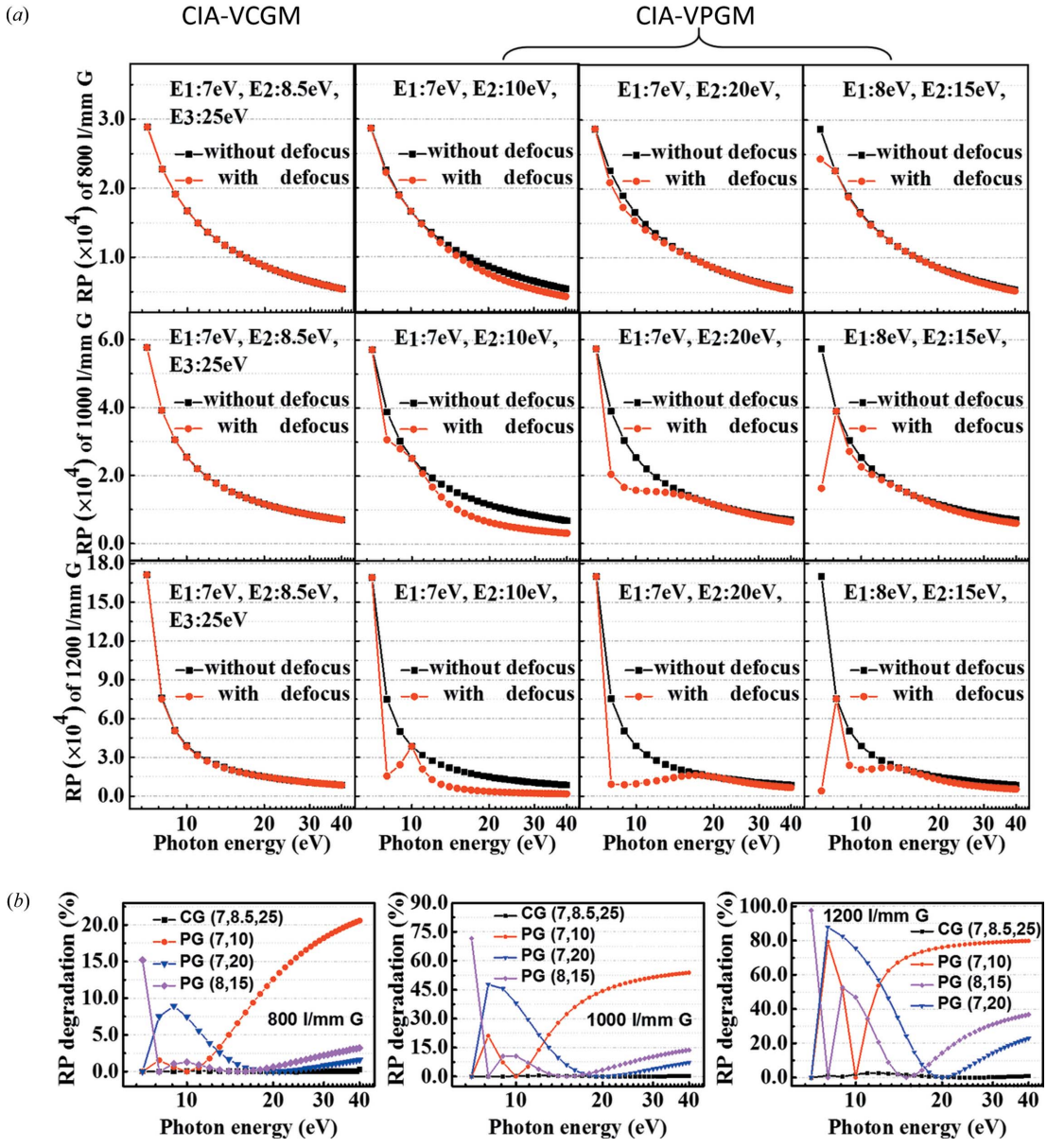

Figure 4
(*a*) Energy resolving power comparison of the CIA-VCGM and the CIA-VPGM with the grating line density as 800 lines mm^{-1}, 1000 lines mm^{-1} and 1200 lines mm^{-1}, where the CIA-VPGM is optimized with different energy sets. The RP without the defocus (black squares) is shown as a benchmark. (*b*) RP degradation caused by the defocus aberration.

Aberration from defocus:

$$\lambda/\lambda_{de} = \frac{2dF_{20}W}{m\lambda}.$$

Aberration from coma:

$$\lambda/\lambda_{co} = \frac{3dF_{30}W^2}{2m\lambda}.$$

Diffraction limit:

$$\Delta\lambda/\lambda_{limit} = \frac{1}{mN}.$$

$$\Delta\lambda/\lambda_{total} = \Big[(\Delta\lambda/\lambda_{so})^2 + (\Delta\lambda/\lambda_{ex})^2 + \big(\Delta\lambda/\lambda_{gr}\big)^2 + (\Delta\lambda/\lambda_{fo})^2 + (\Delta\lambda/\lambda_{de})^2 + (\Delta\lambda/\lambda_{co})^2 + (\Delta\lambda/\lambda_{limit})^2\Big]^{1/2},$$

where β is the diffraction angle, α is the incidence angle, m is the diffraction order, R is the grating radius, s is the exit slit size, d is the grating spacing, r_1, r_2 are the virtual object distance and imaging distance of the grating, Σ_{yV} is the RMS value of the virtual source size ($\Sigma_{yV} = M\Sigma_{yA}$, M is the magnification of the focusing mirror); σ_{gr}, σ_{fo} are the meridian RMS slope errors of the grating and the focusing mirror; W is the half of the illuminated length of the grating and N is the number of coherently illuminated grating grooves.

In each case the RP without the defocus term is shown as a benchmark. Grating line densities higher than 1200 lines mm^{-1} are not considered because the grating incidence angle for them would be larger than 90° at 7 eV according to the grating equation. For the model CIA-VCGM, the RP does not suffer much from the defocus for all gratings. This is easily understood because the defocus aberration is well suppressed in the model CIA-VCGM and the RSW from the defocus aberration does not dominate as shown in Fig. 5. However, for the comparable CIA-VPGM, it is difficult to find a suitable energy set to suppress defocus over a wide VUV energy range. The RP degradation caused by the defocus aberration is shown in Fig. 4(*b*). It can be found that the RP degradation caused by the defocus aberration could be ignored for the model CIV-VCGM.

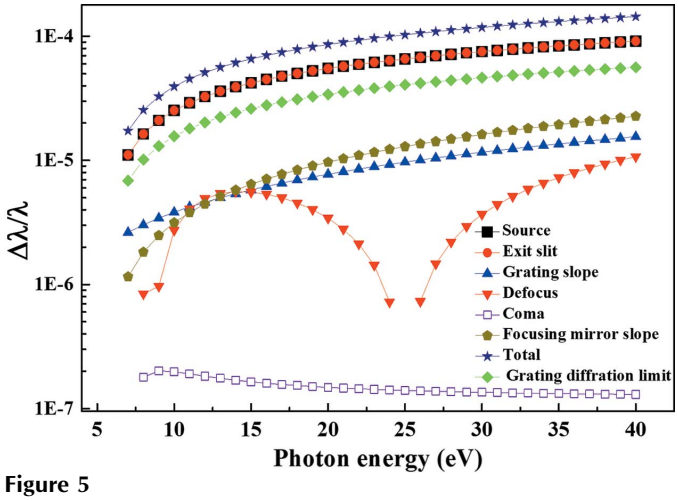

Figure 5
Breakdown of the total RSW (solid stars) of the model CIA-VCGM (with grating line density 1000 lines mm^{-1}) into various components of the exit slit (solid circles), source (solid squares), slope errors of the grating (upward triangles), defocus aberration (downward triangles), slope errors of the focusing mirror (solid pentagons), grating diffraction limit (solid rhombus) and coma aberration (open squares).

The CIA-VCGM with 1000 lines mm^{-1} or 1200 lines mm^{-1} gratings could achieve 0.4 meV energy resolution at 10 eV (Fig. 4). This should lay a solid foundation for a high-performance ARPES beamline, because such an energy resolution from a beamline is five times smaller than the energy resolution of a state-of-art electron analyzer (energy resolution of about 2 meV).

The total RSW and its various components of a 1000 lines mm^{-1} cylindrical grating (Fig. 4*a*) are shown in Fig. 5. It is shown that the defocus aberration is negligible and the extra-focus CIA-VCGM is almost an aberration-free system in this energy range. The largest two contributions to the total energy resolving power are from the source size and the exit slit size. As mentioned above, the exit slit size here is a variable value, which is chosen according to the beamline demagnification, with which the FWHM value of the spot is allowed to pass through the exit slit. The third largest contribution to the RSW is from the diffraction limit $1/N$, where N is the number of coherently illuminated grooves. At an undulator beamline, the included angle for an extra-focus CIA-VCGM is much larger than that for a NIM, which allows the beam incoming with a grazing incidence on the grating. Therefore, the illuminated area on the grating will be much larger than that in the NIM and the contribution from the grating diffraction limit of the CIA-VCGM is much lower than that of the NIM. Yet the benefit of enlarging the illuminated area has to be weighed against the disadvantage caused by increased aberrations. Technically speaking, the slope errors of the cylindrical optics are generally a few times worse compared with the plane optics; nevertheless, the resulting degradation of the RP is marginal. As an example, the RP will be degraded from 5.8×10^4 to 5.2×10^4 at 7 eV with the slope error varying from 0.3 µrad to 1 µrad for the 1000 lines mm^{-1} cylindrical grating. It turns out that the partition contribution to the total RSW from the slope errors in the VUV range is much smaller than that from the source because of the long wavelength.

We would like to stress that the small contribution from the coma shown in Fig. 5 is due to a careful choice of optimization energy. As shown in Fig. 6, the RSW could be much worse for the CIA-VCGM by choosing other energies, because the coma aberration is most severe at 7 eV, whereby the spot size on the grating is at its maximum value.

3. Defocus aberration with different optical lengths

For the CIA-VCGM, it can be seen from Fig. 5 that the largest contribution to the RSW is from the source size and the exit slit size. It is tempting to increase the object distance of the focusing mirror in order to minimize both sizes. However, one should bear in mind that the illuminated length on the grating will be simultaneously enlarged with increased object distance. This has two consequences: (i) the component RSW by grating

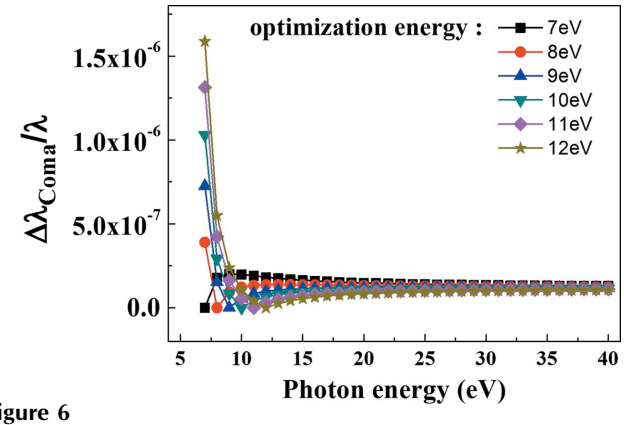

Figure 6
RSW by coma aberration with different optimization energies.

diffraction limit will decrease; (ii) the component by the defocus and the coma will increase: the defocus is proportional to the width of the illuminated length on the grating and the coma is proportional to its square. Fig. 7 shows the dependence of component (exit slit size, source size, diffraction limit, defocus and coma aberration) RSWs and total RSWs on the object distance of the focusing mirror at 14 eV and 40 eV. As seen, even though the defocus and the coma aberrations increase with the distance, they hardly impact the total RSW when the object distance of the focusing mirror is cautiously contained within 30 m.

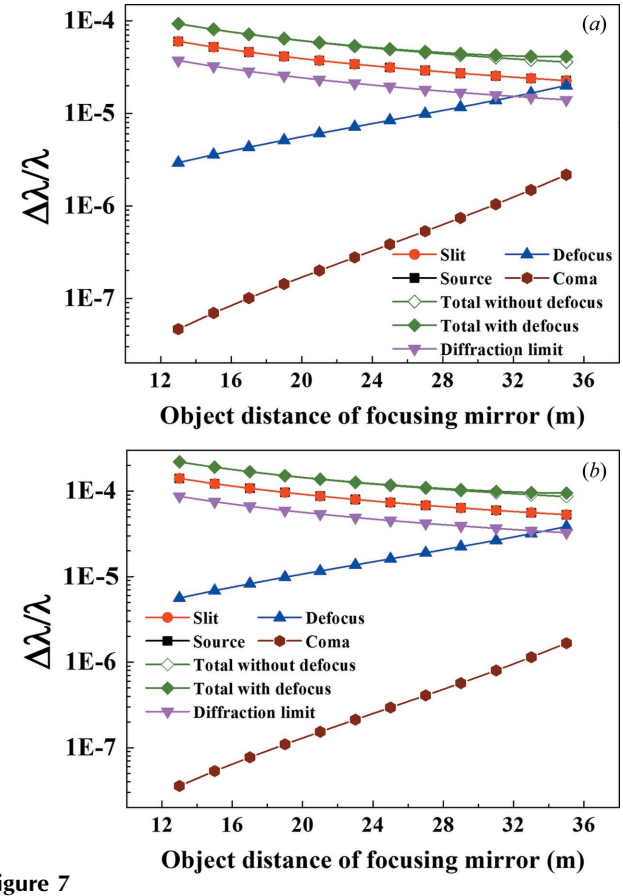

Figure 7
Dependence of component RSWs and total RSWs on the focusing mirror object distance in the CIA-VCGM at (*a*) 14 eV and (*b*) 40 eV.

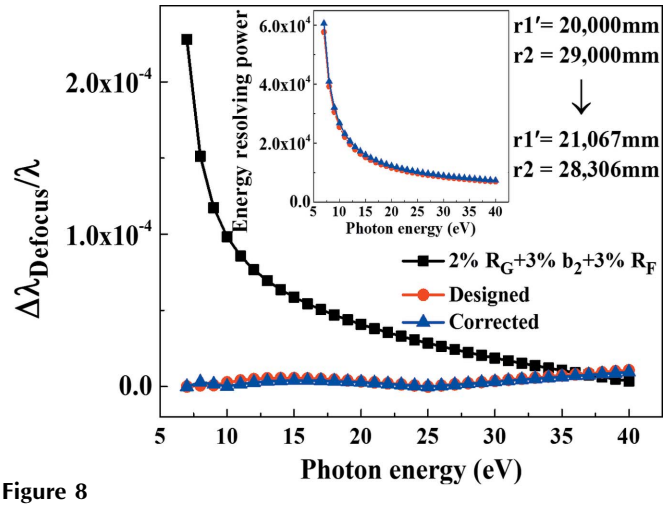

Figure 8
Stability analysis of the CIA-VCGM: the designed defocus aberration (circles); the defocus aberration with 3% errors for focusing mirror radius, 2% errors for grating radius and 3% errors for b_2 coefficient (squares); the corrected defocus aberration (upward triangles) by rearranging the monochromator layout. The upper middle inset shows a comparison between the designed RP and the corrected RP.

4. Stability and efficiency analysis in a CIA-VCGM

4.1. Stability

In practice, the focusing mirror radius R_F, the grating radius R_G and the grating b_2 coefficient have machining errors, and this will cause instability in the monochromator design. Fig. 8 shows that the focus aberration increases considerably with introducing moderate errors (squares): 3% on R_F, 2% on R_G and 3% on the b_2 coefficient. Nevertheless, such effects can be corrected (upward triangles) by properly adjusting the object distance (5.3%) and the imaging distance (2.4%). After correction, the final RP is almost the same as for the original design. The effects of residual measurement errors can be re-corrected online by adjusting the grating incident angle slightly.

4.2. Efficiency

We remark that the total efficiency of the CIA-VCGM is approximately equal to that of the 'dragon' type monochromator because both are constant-included-angle type monochromators, and the incidence angles to the mirrors and their gratings are similar.

5. Influence of beamline setups

The above discussion of an extra-focus CIA-VCGM is based on a simple model monochromator. In reality, the setup of a beamline is far more complicated besides optic principles. For example, the focusing mirror can be placed horizontally or vertically, corresponding to meridional and sagittal focusing mode, for different purposes such as reducing the influence of aberrations in a bending beamline or heat load in an undulator beamline, *etc.* as shown in Figs. 9(*a*) and 9(*b*). Another plane mirror may be needed to deflect the beam to facilitate a required beamline layout. We have carried out ray-tracing

Table 3
Main parameters of the mirrors and the gratings.

Focusing mode	Meridional	Sagittal
Distance from the source to the focusing mirror (mm)	20000	20000
Curvature radius of M1 (mm)	81399	72.9
Deflect angle of M1 (°)	40	3
Distance from the source to the deflecting mirror (mm)	–	21000
Deflect angle of M2 (°)	–	40
Distance from the source to the grating (mm)	20500	22000
Curvature radius of grating (mm)	497663	497663
Imaging distance of grating (mm)	29000	29000

simulations on the two beamline setups with meridional or sagittal focusing mode, respectively, under three energies, 7 eV, 14 eV and 40 eV, whereby 7 eV is the chosen optimization energy, and 14 eV and 40 eV are the energies at which the defocus is the most severe. The parameters in the meridional focusing mode are the same as the basic aforementioned model CIA-VCGM, but they are relisted in Table 3 against some different and important parameters in the sagittal focusing mode.

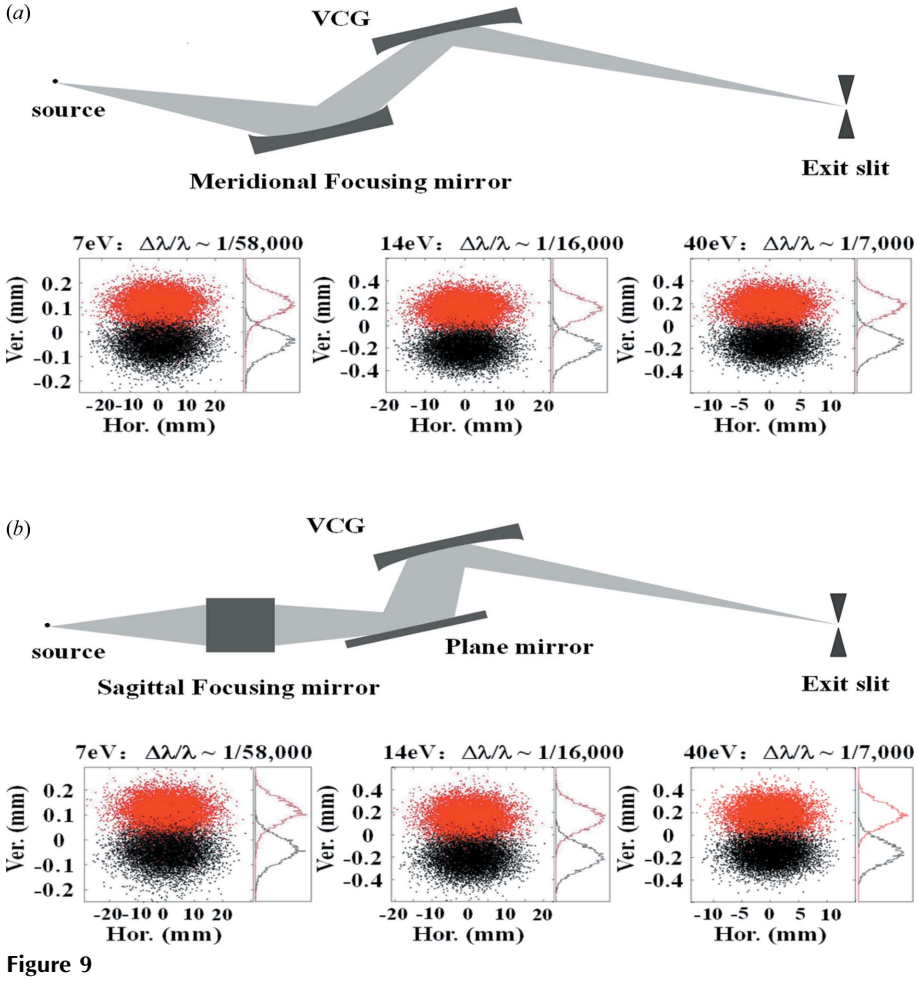

Figure 9
Possible beamline setups and related ray-tracing results: (*a*) meridional focusing mode; (*b*) sagittal focusing mode.

The shadow ray-tracing results are shown in Fig. 9. As demonstrated, both modes can achieve energy resolving powers of 58000 at 7 eV, 16000 at 14 eV and 7000 at 40 eV, matching well with the calculated results (Fig. 4*b*) of the basic model CIA-VCGM (Fig. 1). This is proof of robust behaviour in the energy resolving power of the CIA-VCGM against the adjustment in the beamline setup.

It is a common practice to focus the beam at the exit slits in the non-dispersion direction. To do this, a toroidal mirror could be employed as the focusing mirror in the meridional focusing mode or a sagittal cylindrical mirror takes the place of the planar deflecting mirror in the sagittal focusing mode. Additional slope errors for good optical surface will not significantly affect the RP, as has been discussed for the component RSWs in Fig. 5.

6. Probability of extending the energy range from VUV to soft X-ray

The foregoing discussion is focused on the application of the CIA-VCGM in the VUV range. In fact, because of its strong focusing capability, this monochromator is capable of achieving high performance over an ultra-wide energy range from VUV to soft X-ray using a multi-CIA setup.

As we noticed, the energy resolving power for a single CIA-VCGM is degraded at the high energy end because the included angle is not suitable for higher energy. Therefore, in order to keep the high performance over the whole range, we suggest introducing a multi-CIA setup with different included angles to cover the wider energy range. The different focusing mirrors correspond to different included angles. A few VLS gratings might be mounted in this system. The optical layout of the monochromator is similar to that described in the TDR report of the European XFEL (Sinn *et al.*, 2012). It should be noted that the grating used in the soft X-ray range will have an optimized grating radius R sufficiently large to be equivalent to a plane grating. That is to say, the CIA-VCGM for the VUV range can be combined with a CIA-VPGM for the soft X-ray range. The two monochromators could be easily combined, as their mechanical structures are the same. In addition, it can be found that the beamline setup is compatible with VIA-VPGM as in Fig. 9(*b*). Therefore, an ultra-wide photon energy range could be achieved with the above two schemes.

7. Conclusion

In this report, the design for a new monochromator type (an extra-focus CIA-VCGM) is described for the VUV range. The defocus aberration is well suppressed in the VUV range and a fixed focus spot can be obtained. Therefore, a high-performance (high energy resolving power and high photon flux) monochromator with a fixed exit slit can be realised with few technical difficulties in the VUV range (especially 7–40 eV). Furthermore, this new type of monochromator has the potential to be combined with the current extra-focus CIA-VPGM or VIA-VPGM type to extend its energy range from VUV to soft X-ray.

This work was supported by the National Natural Science Foundation of China (Nos. 11275255, 11205236 and 11005146) and the Open Research Project of Large Scientific Facility from Chinese Academy of Sciences: Study on Self-Assembly Technology and Nanometer Array with Ultra-High Density. The authors thank Professor Y. L. Yan (Institute of High Energy Physics) for his helpful discussions. The authors are also grateful to the X-ray Interference Lithography beamline (BL08U1B) staff for their help.

References

Borisenko, S. V. (2012). *Synchrotron Radiat. News*, **25**, 6–11.
Bostwick, A., Rotenberg, E., Avila, J. & Asensio, M. C. (2012). *Synchrotron Radiat. News*, **25**, 19–25.
Damascelli, A. & Shen, Z. X. (2003). *Rev. Mod. Phys.* **75**, 473–541.
Hettrick, M. C. & Bowyer, S. (1983). *Appl. Opt.* **22**, 3921–3924.
Hettrick, M. C. & Underwood, J. H. (1986). *AIP Conf. Proc.* **147**, 237–245.
Hettrick, M. C. & Underwood, J. H. (1988). US Patent 4 776 696.
Hettrick, M. C., Underwood, J. H., Batson, P. J. & Eckart, M. J. (1988). *Appl. Opt.* **27**, 200–202.
Janowitz, C., Zandt, T., Dudy, L., Manzke, R. & Reichardt, G. (2012). *Nucl. Instrum. Methods Phys. Res. A*, **693**, 160–165.
Kiyokura, T., Maeda, F. & Watanabe, Y. (1998). *J. Synchrotron Rad.* **5**, 572–574.
Lai, L. J., Tseng, P. C., Yang, Y. W., Chung, S. C., Song, Y. F., Cheng, N. F., Chen, C. C., Chen, C. T. & Tsang, K. L. (2001). *Nucl. Instrum. Methods Phys. Res. A*, **467–468**, 586–588.
Ono, K., Ho Oh, J., Horiba, K., Mizuguchi, M., Oshima, M., Kiyokura, T., Maeda, F., Watanabe, Y., Kakizaki, A., Kikuchi, T., Yagishita, A. & Kato, H. (2001). *Nucl. Instrum. Methods Phys. Res. A*, **467–468**, 573–576.
Petaccia, L., Vilmercati, P., Gorovikov, S., Barnaba, M., Bianco, A., Cocco, D., Masciovecchio, C. & Goldoni, A. (2009). *Nucl. Instrum. Methods Phys. Res. A*, **606**, 780–784.
Petersen, H. (1982). *Opt. Commun.* **40**, 402–406.
Pimpale, A. V., Deshpande, S. K. & Bhide, V. G. (1991). *Appl. Opt.* **30**, 1591–1594.
Rah, S.-Y., Kang, T.-H., Chung, Y., Kim, B. & Lee, K.-B. (1995). *Rev. Sci. Instrum.* **66**, 1751–1753.
Reininger, R., Bozek, J., Chuang, Y.-D., Howells, M., Kelez, N., Prestemon, S., Marks, S., Warwick, T., Jozwiak, C., Lanzara, A., Hasan, M. Z. & Hussain, Z. (2007). *AIP Conf. Proc.* **879**, 509–512.
Riemer, F. & Torge, R. (1983). *Nucl. Instrum. Methods Phys. Res.* **208**, 313–314.
Sinn, H., Dommach, M., Dong, X., La Civita, D., Samoylova, L., Villanueva, R. & Yang, F. (2012). *X-ray Optics and Beam Transport*, European XFEL Technical Design Report, ch. 4, p. 51. European X-ray Free-Electron Laser Facility GmbH, 22761 Hamburg, Germany.
Somorjai, G. A. (1981). *Chemistry in Two Dimensions: Surfaces.* Ithaca: Cornell University Press.
Songsiriritthigul, P., Pairsuwan, W., Ishii, T. & Kakizaki, A. (2003). *Nucl. Instrum. Methods Phys. Res. B*, **199**, 565–568.
Strocov, V. N., Schmitt, T., Flechsig, U., Schmidt, T., Imhof, A., Chen, Q., Raabe, J., Betemps, R., Zimoch, D., Krempasky, J., Wang, X., Grioni, M., Piazzalunga, A. & Patthey, L. (2010). *J. Synchrotron Rad.* **17**, 631–643.
Tanaka, K., Lee, W. S., Lu, D. H., Fujimori, A., Fujii, T., Risdiana, Terasaki, I., Scalapino, D. J., Devereaux, T. P., Hussain, Z. & Shen, Z.-X. (2006). *Science*, **314**, 1910–1913.
Terashima, K., Matsui, H., Hashimoto, D., Sato, T., Takahashi, T., Ding, H., Yamamoto, T. & Kadowaki, K. (2006). *Nat. Phys.* **2**, 27–31.
Underwood, J. H. & Gullikson, E. M. (1998). *J. Electron Spectrosc. Relat. Phenom.* **92**, 265–272.
Van Elp, J. (1997). *Nucl. Instrum. Methods Phys. Res. A*, **390**, 403–408.
Xue, L., Reininger, R., Wu, Y.-Q., Zou, Y., Xu, Z.-M., Shi, Y.-B., Dong, J., Ding, H., Sun, J.-L., Guo, F.-Z., Wang, Y. & Tai, R.-Z. (2014). *J. Synchrotron Rad.* **21**, 273–279.
Yan, Y., Shigemasa, E. & Yagishita, A. (1998). *J. Synchrotron Rad.* **5**, 246–251.
Yan, Y. & Yagishita, A. (1995*a*). KEK Report 95–9. KEK, Tsukuba, Ibaraki, Japan.
Yu, X. J., Wang, Q. P., Lu, L. J., Pan, H. B., Xu, F. Q. & Xu, P. S. (2001). *Nucl. Instrum. Methods Phys. Res. A*, **467–468**, 597–600.